Design and optimization of diffraction-limited storage ring lattices based on many-objective evolutionary algorithms

He-Xing Yin[1], Jia-Bao Guan[1], Shun-Qiang Tian[2] and Ji-Ke Wang[1,*]

[1] *The Institute for Advanced Studies, Wuhan University, Wuhan 430072, China*

[2] *Shanghai Advanced Research Institute, Chinese Academy of Sciences, Shanghai 201210, China*

*** Corresponding author. *E-mail address:* jike.Wang@whu.edu.cn

Abstract: Multi-objective evolutionary algorithms (MOEAs) are typically used to optimize two or three objectives in the accelerator field and perform well. However, the performance of these algorithms may severely deteriorate when the optimization objectives for an accelerator are equal to or greater than four. Recently, many-objective evolutionary algorithms (MaOEAs) that can solve problems with four or more optimization objectives have received extensive attention. In this study, two diffraction-limited storage ring (DLSR) lattices of the ESRF-EBS type with different energies were designed and optimized using three MaOEAs and a widely used MOEA. The initial population was found to have a significant impact on the performance of the algorithms and was carefully studied. The performances of the four algorithms were compared, and the results demonstrated that the grid-based evolutionary algorithm (GrEA) had the best performance. MaOEAs were applied in many-objective optimization of DLSR lattices for the first time, and lattices with natural emittances of 116 pm·rad and 23 pm·rad were obtained at energies of 2 GeV and 6 GeV, respectively, both with reasonable dynamic aperture and local momentum aperture (LMA). This work provides a valuable reference for future multi-objective optimization of DLSRs.

Keywords: storage ring lattices • many-objective evolutionary algorithms • GrEA algorithm • NSGA

1. Introduction

Fourth-generation synchrotron radiation light sources, also known as DLSRs [1], have been constructed worldwide. Their natural emittance is approximately one to two orders of magnitude lower than that of third-generation light sources, generally of the order of tens or hundreds of picometers, which is close to the X-ray diffraction limit. DLSRs use a multibend achromat (MBA) structure and strong focusing magnets, which reduce emittance significantly and result in high natural chromaticity. High-strength sextupoles can correct chromaticity well and introduce a large nonlinear force, which can lead to the deterioration of the lifetime and dynamic aperture [2]. Optimizing an accelerator requires fulfilling many objectives, such as achieving low emittance, good nonlinear performance, and excellent

performance. Optimizing them simultaneously is an enormous challenge [3].

The optimization of a DSLR lattice is a nonlinear and intricate problem. Previously, the global scan of all stable settings (GLASS) [4] was used to explore the global linear properties of storage rings and provide a systematic method for finding stable optics. Compared to third-generation light sources, the number of magnets in DLSRs is remarkably higher, and GLASS consumes a significant amount of time. Over the last two decades, MOEAs have been widely used in accelerator optimization [5-9] to determine a set of reasonable solutions for each optimization objective. Among these algorithms, multi-objective particle swarm optimization (MOPSO) [10] and the multi-objective genetic algorithm (MOGA) [11] are the most widely used. Moreover, the High Energy Photon Source (HEPS) [12] study demonstrated that combining the MOGA and MOPSO in a rational way to optimize the lattice can yield better results than using only one algorithm [13].

Recent studies on MOEAs have indicated that classical evolutionary algorithms, such as NSGA-II [14] and SEPA2 [15], are in effective in dealing with many-objective optimization problems (MaOPs) if the number of objectives is four or more, owing to a decrease in the selection pressure on the Pareto front [16, 17]. When the dimensionality of the objective space increases to four or more, all solutions in a population become non-dominated solutions in previous generations [18]. This degrades the performance of these algorithms, possibly even to the point of a random search. Because an increase in the number of objectives exponentially increases the number of non-dominated solutions in the population, the effectiveness of the crowding distance method [19] of NSGA-II and other selection mechanisms to ensure population diversity is reduced, causing the algorithms to converge prematurely and fall into local optima [20].

MaOEAs have received considerable attention in recent years [21]. Various methods have been proposed to effectively enhance the performance of evolutionary algorithms in handling MaOPs. These approaches can be roughly classified into five types [22]: Pareto-dominance modification, indicator, decomposition, grid, and diversity-emphasis. Using these approaches, several MaOEAs can effectively solve MaOPs.

In the accelerator field, the Shanghai soft X-ray free-electron laser (SXFEL) has applied NSGA-III [23], an MaOEA, to optimize the overcompression mode in the linac for producing large-bandwidth XFEL pulses [24]. Using decomposition, NSGA-III determines a well-distributed hyperplane and associates all solutions with the reference points in this hyperplane to enhance the selection pressure and maintain diversity for solving MaOPs. The SXFEL experiment demonstrates that NSGA-III significantly outperforms NSGA-II in the case of more than three objectives. However, the performance of NSGA-III

varies for different test problems and is even worse than NSGA-II for some problems [25]. To further study the performance of MaOEAs in the accelerator field, additional algorithms must be developed and experiments must be conducted.

The MOGA is not independent of the distribution of the initial population [13] and requires a good distribution of the initial population to converge to the true global optima [26]. A stable periodic solution for a lattice is called a stable solution, and a stable solution that satisfies these constraints is called a feasible solution. A DLSR uses many magnets, and finding a stable or feasible solution using a vast number of magnet combinations is difficult. In this study, the number of variables for the 2 GeV ring was 28, and each variable was changed once, producing 2^{28} magnet combinations. On average, 100 thousand randomly generated solutions produce only 10–15 stable solutions, of which only an extraordinarily small number are feasible. Assuming that the proportion of feasible solutions in the population in the early optimization stage is very small, these solutions and their feasible offspring will dominate all the remaining infeasible solutions. Eventually, all solutions in the population will be generated from these solutions, thus reducing the diversity of the population and leading algorithms to converge to the local optima.

In this study, many-objective optimization of DLSR lattices is performed for the first time, and the performances of four different algorithms are compared in terms of many-objective optimization. Two DLSR lattices and strategies for their optimization are described in Section 2. The effects of the initial solutions obtained using three different methods on evolutionary algorithms are discussed in Section 3. The multi-objective optimization results with four different algorithms for the 2 GeV ring are presented and analyzed in Section 4. Section 5 presents the results of the multi-objective optimization of the 6 GeV ring. The conclusions are summarized in Section 6.

2. Method

2.1. Designed Lattices

To evaluate the performance of different algorithms on the MaOPs of DLSR lattices, two lattices were designed with energies of 2 GeV and 6 GeV. The magnetic arrangement of one cell of the 2 GeV ring lattice is shown in Fig. 1 (top). The lattice was designed with a circumference of approximately 300 m and an H7BA focusing structure [27], which has 12 cells and provides 12 identical straight sections with a length longer than 5.3 m. In addition to the H7BA structure, the focusing cell comprehensively uses reverse bends (RBs) [28] and longitudinal gradient bends (LGBs) [29] with transverse focusing to reduce beam emittance as much as possible. The focusing structure uses the ESRF-EBS scheme [27], in which

the space between two pairs of dipoles, the first and second and the sixth and seventh, is expanded to correct the natural beam chromaticity with weakened sextupoles because of the dispersion bump. The main magnets of each cell include seven combined transverse and longitudinal gradient dipoles, ten quadrupoles, four RBs, and six quadrupoles. As shown in Fig. 1 (bottom), a focusing quadrupole other than that of the 2 GeV ring is positioned next to the purple sextupole of the 6 GeV ring because storage rings with higher energy require a stronger focusing force. The lattice of the 6 GeV ring, which has 48 cells, has an approximate circumference of 1350 m.
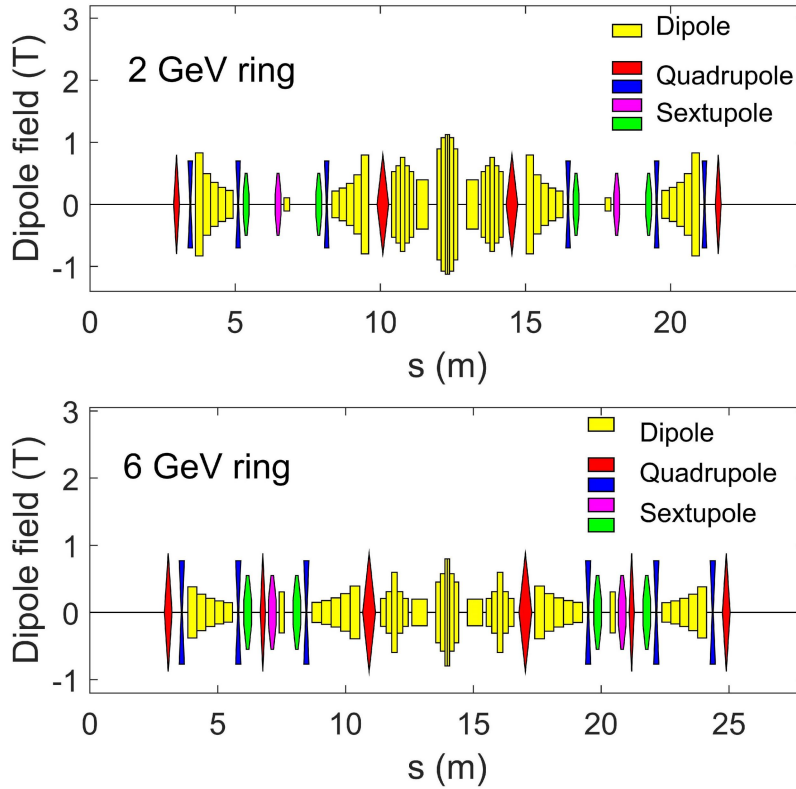
Fig. 1. Magnet layout of one cell each of 2 GeV and 6 GeV ring lattices. The vertical coordinate indicates the dipole field. For visualization convenience, the heights of the focusing quadrupole, defocusing quadrupole, and sextupoles are set to different fixed values, where red and purple indicate focusing and blue and green indicate defocusing.

The 2 GeV and 6 GeV rings had 28 and 29 variables, respectively. For the 2 GeV ring, the maximum strength of the dipoles was 1.2 T; the maximum gradient of the independent quadrupoles was 60 T/m; and the maximum gradient of the combined magnets was 40 T/m. The corresponding maximum limits for the 6 GeV ring were 1.5, 80, and 60 T/m, respectively. As shown in Table 1, $K1$ is the gradient of the independent quadrupole and is combined in RBs; $K2$ is the gradient combined in dipoles; RBA is the

angle of the RBs; LA is the longitudinal gradient distribution coefficient of each dipole, where the first dipole has the same distribution coefficient as the second; assuming that the angles of the four different dipoles in a cell are A, B, C, and D, MB is the angular distribution coefficient, which for A, B, C, and D is denoted by a, b, c, and d, respectively, where the ratios a:b:c:d = A:B:C:D; LB is the length of each dipole; and LD is the deviation of distances between different dipoles, while these distances are set to fixed values at the beginning of

Table 1. Variables of the two DLSR lattices and their ranges.

| Variables	Number		Values		Units
	2 GeV	6 GeV	2 GeV	6 GeV	
K1	7	8	<60	<80	T/m
K2	4		<40	<60	T/m
RBA	2		<0.045/0.090	<0.004/0.008	rad
LA	3		<10		...
MB	4		...		...
LB	4		[0.5, 1.5]	[0.6, 1.8]	m
LD	4		...		m

2.2. Algorithms

The benchmark algorithm used in this study was NSGA-II, and the other three MaOEAs were GrEA [30], NSGA-III, and MOEA/D [31]. The flowcharts of these algorithms are shown in Fig. 2, and they are described below.

NSGA-II is a non-dominated sorting algorithm based on crowding distance, and its basic framework is described below. First, for a given initial population Q with a fixed size N, the offspring population S with the same size is generated by selection, crossover, and mutation. Then, N non-dominated solutions are selected from the merged populations of Q and S according to non-dominated sorting [23] and crowding distance as the new population Q. These steps are repeated until the algorithm converges or reaches the maximum number of iterations.

The GrEA is a grid-based algorithm used for MaOPs. Its basic algorithm framework is similar to that of NSGA-II. It introduces a grid mechanism to enhance the convergence and diversity of the algorithm. The non-dominated sorting method in NSGA-II is replaced by grid dominance and grid difference, which effectively strengthen the convergence pressure to determine the Pareto front. Additionally, the

fitness assignment process is revised through three grid-based criteria: grid ranking (GR), grid crowded distance (GCD), and grid coordinate point distance (GCPD).
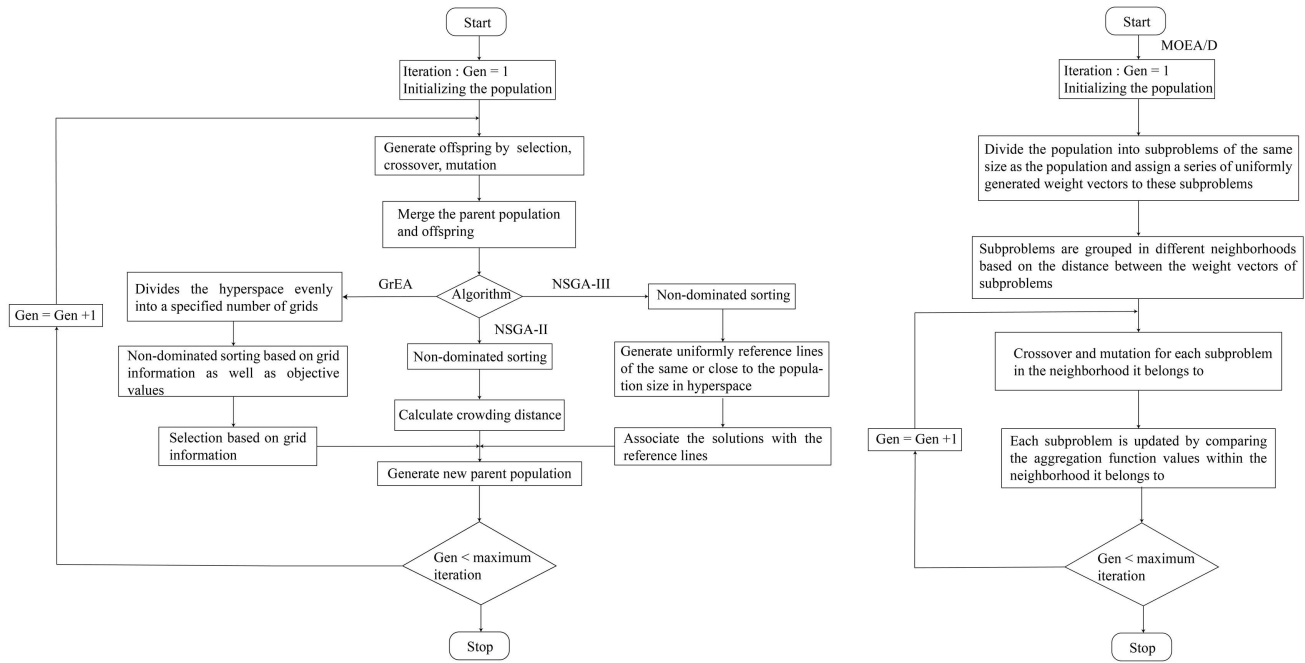
Fig. 2. Flowcharts of the four algorithms. NSGA-II, GrEA, and NSGA-III have a similar framework and are shown in a single flowchart (left). MOEA/D is shown on the right.

NSGA-III is an improved version of NSGA-II, which solves MaOPs by modifying the crowding distance operator. All steps in NSGA-III other than the step involving the crowding distance operator are the same as those in NSGA-II. Instead of the crowding distance operator, NSGA-III uses the following steps: First, many well-distributed reference points are generated using Das and Dennis's systematic approach [32] to maintain diversity. Each population member is then associated with its nearest reference line after standardization. Finally, non-dominated solutions close to the reference line are given a higher priority.

MOEA/D uses uniformly distributed weight vectors to decompose a multi/many-objective problem into a series of single-objective sub-problems and optimizes them simultaneously. Each subproblem is optimized and updated with information regarding its corresponding neighborhood, which is determined by the distance between the individual weight vectors. Several aggregation methods, such as the weighted sum (WS) [33], Tchebycheff [33], and penalty-based boundary intersection (PBI) [34], are used to aggregate the individual objective values in MOEA/D.

Three metrics, *SumMin, MinSum,* and *Range,* were used to evaluate the performance of the MaOEA

[35]. Assume MaOPs, where the optimal value of each objective is the minimum value, *SumMin* is the sum of the minimum values of each objective in the population, which characterizes the convergence to the Pareto front edge, and *MinSum* is the minimum value of the sum of the individual objectives in the population, which characterizes the convergence to the Pareto front center. Smaller values indicate better convergence. *Range* is the sum of the range of objective values for each objective in the population, which characterizes the diversity of the population. The larger the value, the better the diversity. For clarity, the values of the three metrics were divided by the number of objectives.

The inverted generational distance (IGD) [36] and hypervolume (HV) [37] are widely used as metrics to compare the performance of various MaOEAs. However, the calculation of the IGD requires knowledge of the true Pareto front; therefore, it was not used in this study. HV measures the combined performance of convergence and diversity, with a larger HV indicating better performance.

In this study, the HV was the main metric for evaluating the performance of the different algorithms, and the other three metrics were used as supplements.

2.3. Strategy

To obtain high performance and good stability, the natural emittance, dynamic aperture, LMA, and the brilliance at the central bending magnet and center of the straight section were selected as the optimization objectives in all multi-objective optimizations. Although emittance and brilliance are not independent objectives, they can be used simultaneously as optimization objectives. This is because brilliance is not only related to the emittance but is also closely related to the beam optics at the source point. A lattice with a larger emittance may have higher brilliance if the former has a smaller β function at the source point. Moreover, several light sources have been implemented or proposed to replace the central bending magnet with a superbend to obtain higher-energy photons, such as DIAMOND [38], ALS-U [39], SLS-II [40], Sirius [41], and WHPS [42]. Therefore, using the brilliance at the central bending magnet as an objective is reasonable. In the following experiments, all calculations and simulations were performed using AT [43].

The two important characteristics of a storage ring are brilliance and coherence, and a very effective way to improve them is to reduce its natural emittance. Therefore, the natural emittance ε_x was used as an optimization objective. A lattice with an extremely small emittance is likely to be impractical because the dynamic aperture and LMA may be too small for beam injection and beam lifetime. The area of the dynamic aperture without energy deviation was used as the optimization objective and is denoted

as DA. A sufficient LMA is typically required to obtain the desired beam life. The LMA determined by the transverse beam dynamics tends to be small at locations with large dispersion invariants, such as the arc of the H7BA cell. In fact, the LMA is usually limited by transverse dynamics only in the arc and by the RF bucket height elsewhere. It tends to be the largest at the center of the straight section and the smallest at the position with maximum dispersion. The LMA at these two positions was obtained by tracking 1000 turns. The average of the LMA at the above two positions was used as the LMA optimization objective and is denoted as δ [26]. The light drawn from the bending magnet can have a higher energy, and its brilliance [44] is

$$B(\omega) = \frac{N_{Flux}(\omega)}{(2\pi)^{3/2}\sigma_x\sigma_y\sigma_{Y'}}, \quad \sigma_{Y'}$$
$$= \sqrt{\sigma_{y'}^2 + \sigma_{r'}^2}, \quad (1)$$

where N_{Flux} is the peak photon flux of the beam; ω is the oscillation frequency; $\sigma_{x,y}$ represent the bunch size in the horizontal or vertical direction; $\sigma_{Y'}$ is the effective vertical divergence; $\sigma_{y'}$ is the vertical beam divergence; and $\sigma_{r'}$ is the vertical opening angle of synchrotron radiation. In this study, the brilliance of the center dipole BriB was used as an objective, and it was measured when the frequency ω was equal to the characteristic frequency ω_c, the beam current was 200 mA, and the coupling ratio, defined as the ratio of the vertical emittance to the horizontal emittance, was 10%. An insertion device is installed at the center of the straight section to generate synchrotron radiation. Its brilliance [44] is given by

$$B(n)$$
$$= \frac{N_{Flux}(n)}{4\pi^2\sigma_{Tx}\sigma_{Ty}\sigma_{Tx'}\sigma_{Ty'}}, \quad (2)$$

$$\sigma_{Tx,y} = \sqrt{\sigma_{x,y}^2 + \sigma_r^2}, \quad \sigma_r$$
$$= \frac{1}{4\pi}\sqrt{\lambda_n L_{ID}}, \quad (3)$$

$$\sigma_{Tx',y'} = \sqrt{\sigma_{x',y'}^2 + \sigma_{r'}^2}, \quad \sigma_{r'} = \sqrt{\frac{\lambda_n}{L_{ID}}}, \quad (4)$$

where n represents the nth harmonic of the central light cone; $\sigma_{Tx,y}$ and

$\sigma_{Tx',y'}$ are the root mean square deviations of the transverse position and angle in horizontal or vertical direction; $\sigma_{x'}$ is horizontal beam divergence; λ_n is undulator period and L_{ID} is undulator length. Brilliance BriU was generated by an undulator with a length of 200 cm, period of 25 mm, and K value of 1.5 at the center of the straight section when the beam current was 200 mA and the coupling ratio was 10%. By changing the sign of the variable, all objectives were between the minimum value and optimal value during the optimization process. The objectives are denoted as ε_x, $-DA$, $-\delta$, $-BriB$, and $-BriU$ in the text.

Bending magnets inevitably produce dispersion that separates the off-energy orbit from the ideal trajectory. The high-frequency accelerating cavity and insertion devices were mounted in a straight section, and energy deviations were introduced. To minimize the coupling of energy variations to the transverse oscillations, the dispersion of the straight section for the beam lines was matched to zero when the multi-objective optimization was performed. Before calculating the dynamic aperture and LMA, the horizontal and vertical chromaticity were corrected to +1 if the momentum compaction factor was greater than 0; otherwise, it was corrected to -1. In addition to the limitation of the variable due to the power supply, the following constraints were imposed:

(1) The values of the natural emittance and tune should be real numbers to ensure that the solution is stable.

(2) The maximum β in the horizontal and vertical directions should not be more than 30 m.

In the experiments described below, a simulated binary crossover and polynomial mutation were used in the genetic operator, and their settings were the same for each algorithm. For each optimization, the initial population size was 1000. In the various algorithms, the specific parameters were set as follows: The number of grids for GrEA was nine; the number of reference points in NSGA-III was the same as the population size; the aggregation function used for MOEA/D was the Tchebycheff function; and the neighborhood size was set to 1/10 of the population size, that is, 100.

3. Optimization results with different initial populations

The results of the initial multi-objective optimization of the 2 GeV ring showed that most of the solutions in the first 100 generations of each algorithm were infeasible and that the minimum value of the natural emittance of the final optimization result was greater than 250 pm·rad, which was much larger than the expected value. Almost no feasible or stable solutions existed for the initial population. Because this optimization involved 28 variables, the probability of randomly generating a stable solution within

the range of the variables was almost zero, which led to a search for stable and feasible solutions in the early stages of optimization. After one or several feasible solutions were found, only those that dominated the other solutions were used to determine the search direction. This caused the solutions to become trapped in local optima.

In this section, three approaches were used to generate the initial population. In the first approach, the initial feasible solution was generated by the transport line design, as follows: One cell of the storage ring was used as the transport line, and the initial beam optical function was input at the initial point. As the initial point was the center of the straight section and the center of the straight section was the symmetry point, β_x and β_y were chosen to be suitable small values, and η_x, β'_x, β'_y, and η'_x were set to zero for the initial beam optical function. As the transport line did not consider a periodic solution, the question of whether a solution was stable did not arise. Then, each variable was changed one by one until the subsequent beam's optical distribution met the following criteria: the beam optics inside the dipoles meet the low-emittance requirement; the distribution of the dispersion bump is suitable; and the output beam optical function is equal to or close to the initial beam optical function. After the first feasible solution was obtained, sufficient solutions were seeded into the initial population.

In the second approach, a certain number of feasible solutions were found, and the initial population was generated by seeding them. Many solutions were randomly generated in the range of variables, and all solutions satisfying the constraints in Section 2 were feasible. However, only 63 feasible solutions were found in the 200 million randomly generated solutions, which took a total of 23 h 45 min with 200 Xeon 2.4 GHz CPUs in the Supercomputing Center of Wuhan University cluster. The initial population was then seeded with these feasible solutions to save time and computing power. In the third approach, sufficiently stable solutions were searched for and selected directly as the initial population. Twenty million solutions were randomly generated within the appropriate ranges of the variables, and all stable solutions among them were found. A total of 2365 stable solutions were found in 2.4 h with the same CPUs described above, of which 1000 were randomly selected as the initial population.

To investigate the effect of the initial population on the algorithms, natural emittance and dispersion were used as optimization objectives. NSGA-II was used to optimize them, and the maximum number of iterations was 300. As shown in Fig. 3, the results of the third approach at the 100th generation were much worse than those of the other two, and its solutions on the Pareto front were rare. The initial solutions generated by the third approach were randomly generated stable solutions, most of which did not satisfy the given constraints and led to a search for feasible solutions in early optimization and poor

population diversity. For different generations, the first approach always had the best Pareto front, and the second approach was the second best. The first approach had the best performance because its initial solution was seeded with a solution with low-emittance characteristics and zero dispersion; however, it did not necessarily perform equally well in optimizations with more than three objectives.
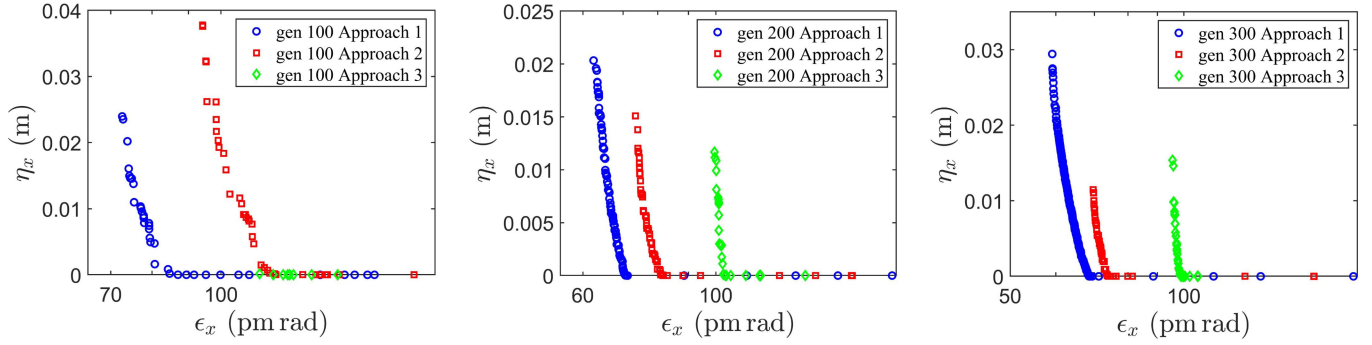

Fig. 3. The Pareto front for two objectives, natural emittance and horizontal dispersion at the center of the straight section obtained with NSGA-II, for different generations and initial populations generated by three approaches.

Table 2. Diversity and convergence metrics for the last generation corresponding to different approaches.

	SumMin	MinSum	Range	HV
Approach 1	0.2594	0.5386	0.7406	0.0494
Approach 2	0	0.4036	0.8627	0.1322

The first and second approaches produced different initial populations, which were then subjected to multi-objective optimization using NSGA-II with a maximum of 250 iterations. The algorithm converged in the last iteration. The data in Table 2 show the results after normalizing each objective value between zero and one. This normalization was also performed for all subsequent results. As shown in Table 2, *SumMin* in the second approach was 0, which indicates that the second approach yielded smaller values for each objective as well as for its *MinSum*. The *Range* and HV of the second approach, on the other hand, were larger. Figure 4 shows that the second approach had a smaller lower bound and broader distribution, which is consistent with the metric results above. We also studied the effect of different approaches on other algorithms and found that it was similar to the effect on the NSGA-II. These results show that the performance of the second approach in multi-objective optimization is better

than that of the first approach.
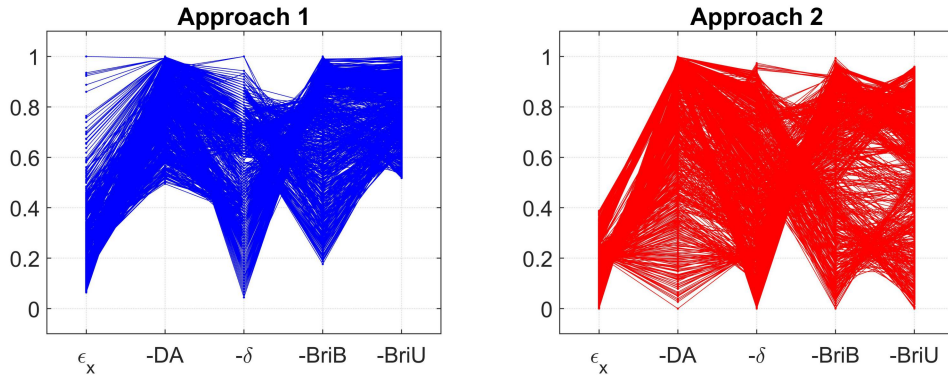
Fig. 4. Parallel coordinate plots of all solutions corresponding to two approaches for the last generation. The horizontal coordinates represent the individual objectives, the vertical coordinates represent the magnitudes of the normalized objective values, and each line represents a solution.

Although the first approach had the best performance in two-objective optimization, it did not perform as well as the second approach in multi-objective optimization. The initial population generated by the first approach was seeded with only one feasible solution, such that the variable space of the population was around this initial solution and smaller than that of the second approach. The second approach produced a larger variable space for the initial population, which yielded better results in multi-objective optimization. When the number of variables is large, leading to a large variable space, none of the randomly generated stable solutions are likely to be feasible, or only a few of them are. This can cause a reduction in population diversity and trap the algorithm in local optima. To find global optimal solutions, sufficient time must be spent finding additional initial feasible solutions for significant variable space problems. Therefore, the second approach was used to generate the initial population for the subsequent experiments. Recently, machine learning techniques have been used as substitutes for simulations to evaluate solutions in optimization algorithms [45, 46]. If machine learning is used, then the computational resource consumption required for the second approach is likely to be significantly reduced. Furthermore, incorporating machine learning into the iterative process of evolutionary algorithms can lead to significant reductions in the required computational resources and potentially yield better results.

4. Optimization results for the 2 GeV ring

4.1. Results

In this section, the results of the many-objective optimizations of the 2 GeV ring lattice using four different evolutionary algorithms are described. The maximum number of iterations was set to 250 because all algorithms converge at the 250th iteration. Table 3 shows that the algorithms, in descending order of *HV,* were GrEA, NSGA-III, NSGA-II, and MOEA/D. Thus, GrEA showed the best combined performance in terms of convergence and diversity. Furthermore, the ascending order of *SumMin* and *MinSum* and the descending order of *Range* were the same as above, as shown in Table 3. As shown in Fig. 5, GrEA had the smallest lower bound for all objectives and was the most widely distributed; NSGA-III was second; MOEA/D had a very high lower bound, and the solutions were distributed in a narrow region. This indicates that the GrEA exhibited the best performance, followed by NSGA-III, NSGA-II, and MOEA/D.

**Table 3.** Diversity and convergence metrics of four algorithms for the last generation.

	SumMin	*MinSum*	*Range*	*HV*
NSGA-II	0.0803	0.4360	0.9149	0.0836
GrEA	0.0046	0.4191	0.9648	0.1239
NSGA-III	0.0291	0.4307	0.9410	0.0909
MOEA/D	0.3585	0.5389	0.5007	0.0516
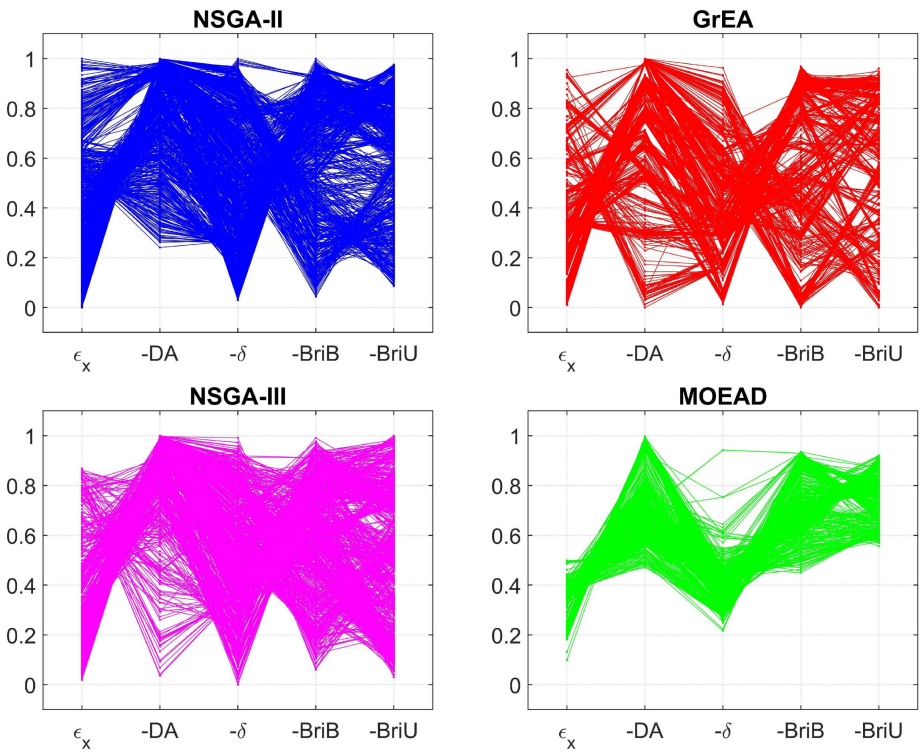
Fig. 5. Parallel coordinate plots of all solutions for four algorithms in the last generation.

Figure 6 illustrates the projection of the Pareto fronts obtained by the four algorithms in the last generation. Overall, the performance of NSGA-III was close to but slightly worse than that of GrEA. When the emittance was less than 100 pm rad, the dynamic apertures of all the solutions were so small that the particles could not survive in the long term. When the emittance was in the preferred interval of 100–150 pm rad, where the solutions are more relevant for practical requirements, the maximum dynamic aperture, LMA, and BriB were obtained using GrEA. The BriU obtained using GrEA was close to that obtained using NSGA-III and larger than the corresponding values from the other two algorithms. When the emittance was between 250 and 350 pm rad, the dynamic aperture obtained using NSGA-II was significantly smaller than that obtained using GrEA and NSGA-III; however, the BriU was high. This suggests that NSGA-II did not maintain diversity in this emittance interval, resulting in a very small β-function at the center of the straight section for solutions with a small dynamic aperture and high BriU. A large dynamic aperture and high BriU in this emittance interval could be obtained when GrEA was used, which indicates that GrEA could better maintain diversity. The solutions of MOEA/D were clustered in a small region, which indicates their poor ability to maintain diversity, causing the algorithm output to fall into local optima. The results in the objective space show that GrEA performed the best, NSGA-III was slightly inferior, and MOEA/D performed the worst, which is consistent with the metrics used to evaluate the performance of the algorithms.
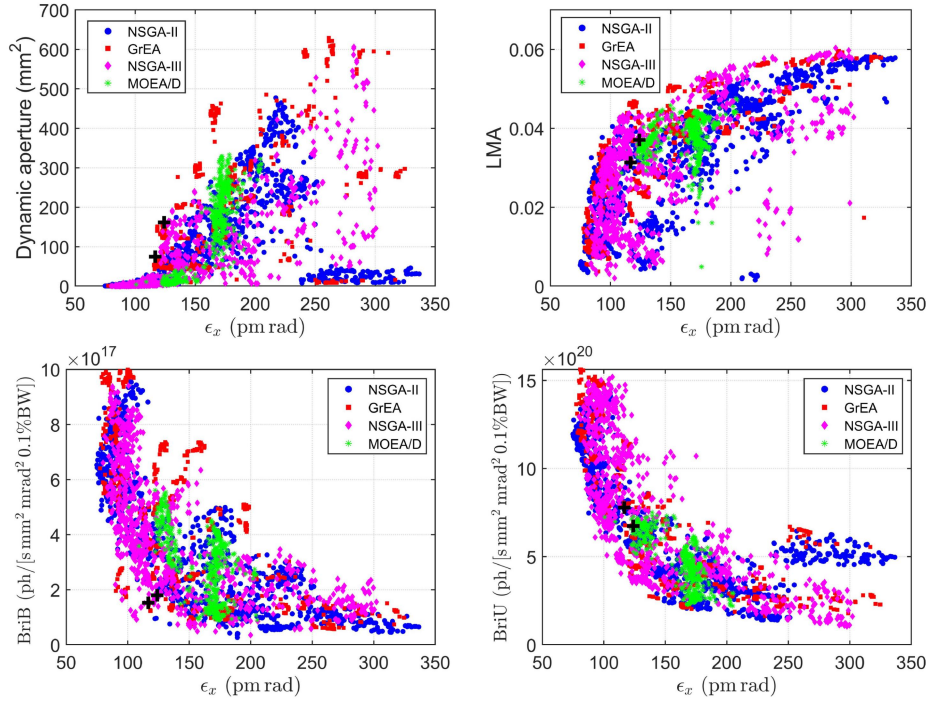
Fig. 6. Projection of the Pareto fronts obtained by four algorithms at the last generation. Black crosses represent two selected lattices.

Because an increase in the number of objectives causes the number of non-dominated solutions to increase exponentially, all solutions in the population from approximately the 30th generation were non-dominated solutions. Choosing the best or preferred solution from among many solutions is a very difficult task. In this study, feature extraction was used to determine the preferred solution. Natural emittance, the smaller of the positive or negative maximum horizontal dynamic aperture, maximum vertical dynamic aperture, minimum LMA in the entire ring, as well as at the center of the straight section, and brilliance at the center of the straight section, as well as at the central bending magnet, were extracted as features and sorted in ascending order of natural emittance. Through feature extraction, the information about each solution can be observed directly, such that the desired solutions can be easily selected. With a sufficient dynamic aperture and LMA, solutions with smaller emittance and higher brilliance are preferred. Two competing solutions were selected based on the feature extraction of the last generation of the GrEA. The beam optics of these two lattices are shown in Fig. 7, whose natural emittances are 116.70 pm·rad and 124.00 pm·rad, respectively. Figure 8 shows that the horizontal dynamic aperture of the first lattice without energy deviation reached 7.5 mm and the vertical aperture reached 3.7 mm, whereas the corresponding values for the second lattice were 7.8 and 6.8 mm, respectively. Both lattices had a certain dynamic aperture for particles with a ± 2% energy deviation. As

shown in Fig. 9, the LMAs of both lattices at the center of the straight section were sufficiently large, and the minimum LMAs in one cell are both larger than 2%.
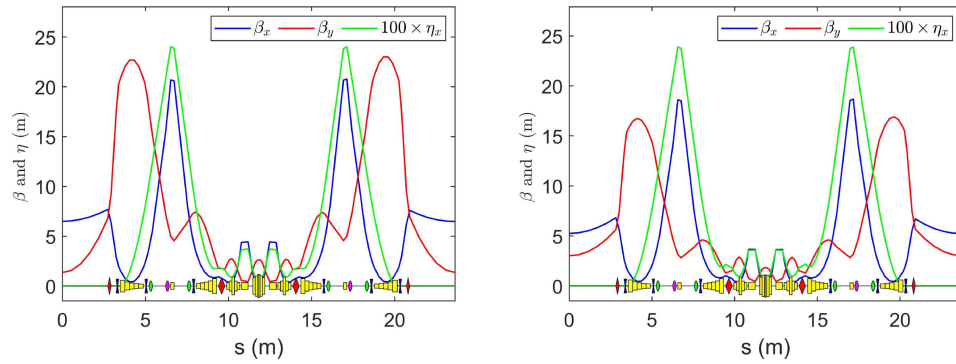
Fig. 7. Beam optics of two selected 2 GeV ring lattices, the first with a natural emittance of 116.70 pm·rad and circumference of 283.71 m, and the other with a natural emittance of 124.00 pm·rad and circumference of 284.87 m.
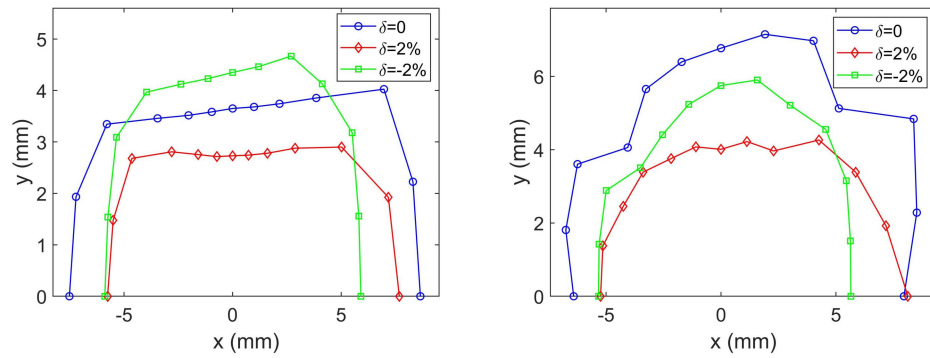

Fig. 8. Dynamic apertures of two selected 2 GeV ring lattices with different energy deviations at the center of the straight section.
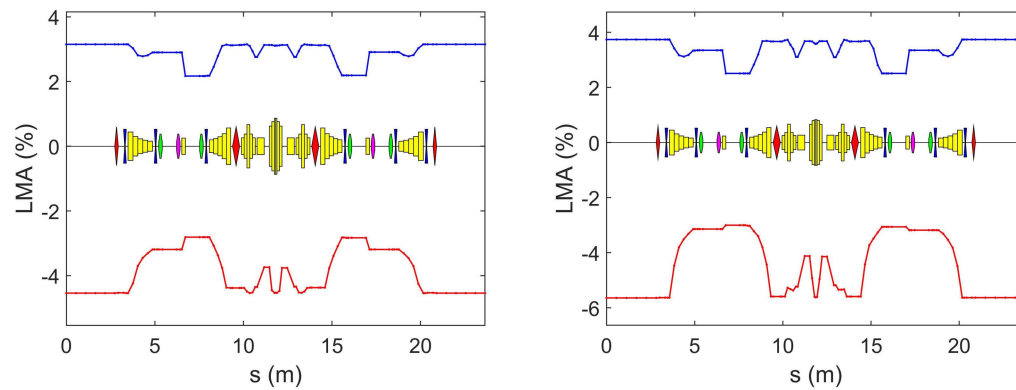
Fig. 9. Local momentum apertures within one cell of the two selected 2 GeV ring lattices.

4.2. Discussion

Because diversity represents the size of the exploration space, the greater the diversity, the larger the exploration space and the higher the probability of finding better solutions, which leads to better convergence. MOEA/D divides the population into T neighborhoods, and solutions only crossover and update the neighborhoods to which they belong. If one solution performs better in a problem that has another solution, the other solution is replaced by this one. Because optimization of the 2 GeV ring is a problem with stricter constraints, only a small number of solutions in the initial population are feasible. This means that these feasible solutions replace all infeasible solutions in the early evolutionary stage, which leads to a significant decrease in the number of solutions that are unique to the population. As shown in Fig. 10, the number of unique solutions in the population of MOEA/D was small in the early evolutionary stage. After approximately 50 generations, the number of unique solutions fluctuated between 400 and 600, whereas the unique solutions of the other three algorithms were close to 1000 for all generations. Therefore, the small number of unique solutions in MOEA/D leads to a significant decrease in diversity, which severely degrades its performance.
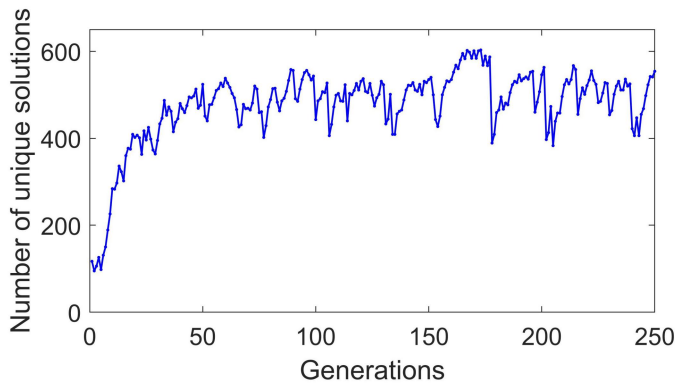
Fig. 10. Number of unique solutions in population with different generations of MOEA/D.

NSGA-III uses the achievement scalar function (ASF) [47] to calculate the extreme points corresponding to each objective axis and then forms a hyperplane through these points, as shown on the left in Fig. 11. All the solutions were normalized by dividing the intercepts formed by this hyperplane by each objective axis. After normalization, the reference points uniformly distributed on the hyperplane intersecting each objective axis with an intercept of 1 were connected to the origin to form a series of reference lines. The process of generating reference lines in a two-dimensional objective space is shown

on the right side of Fig. 11. NSGA-III balances diversity and convergence based on the relationship between solutions and reference lines. Therefore, the ability to find a suitable hyperplane directly determines the performance of NSGA-III.
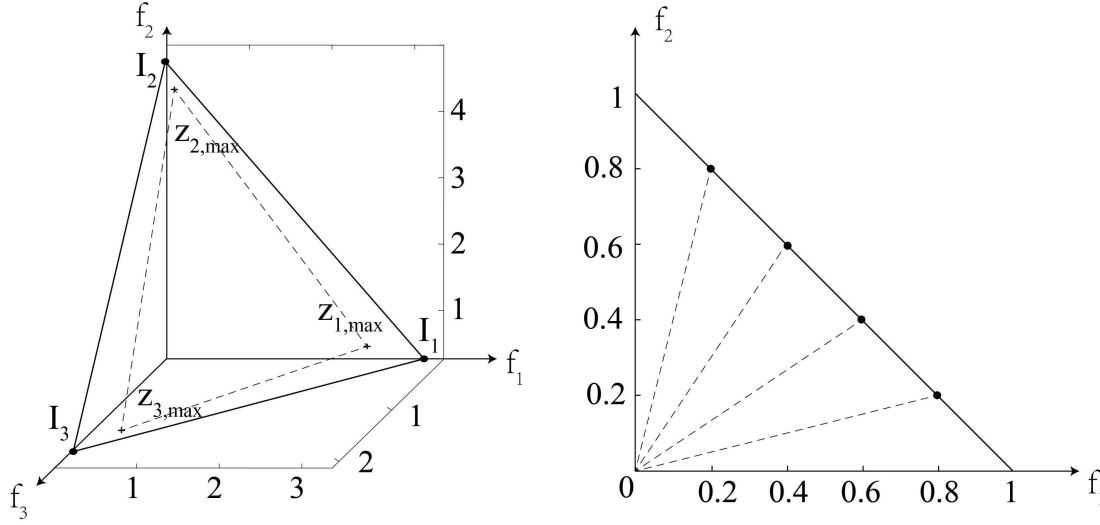

Fig. 11. Schematic of the calculation of the intercepts formed by the hyperplane passing through the extreme points in a three-dimensional objective space (left), where $z_{i,\,max}$ represents the extreme point corresponding to the i-th objective axis and I_i represents the intersection of the hyperplane formed by the extreme points with the i-th objective axis. Uniformly distributed reference points are used to form reference lines through the origin in a two-dimensional objective space (right) for a uniform division of objective space.

As the optimization objectives for the DLSR lattices increase, the shape of the objective space becomes more complex. Consequently, the ASF encounters the problems of a negative intercept and an inability to determine a hyperplane, as mentioned by Deb et al. [48]. In this study, we used the maximum of the non-dominated front (MNDF) [48] instead of the ASF to determine the hyperplane. The MNDF was used to determine the hyperplane by considering the maximum value of each objective of the Pareto front as the intercept corresponding to each objective axis. Although MNDF was used as a substitute for ASF to determine the hyperplane, NSGA-III did not perform as well as GrEA, probably because the hyperplane found by MNDF did not allow NSGA-III to operate at full capacity. Identifying a hyperplane in a complex objective space that allows the mechanism of NSGA-III to function perfectly is difficult and requires further research.

The GrEA divides the hyperspace into a specified number of grids. Solutions closest to the ideal point or closest to the endpoint of the grid closest to the ideal point are given higher priority to enhance

the selection pressure. To increase diversity, solutions with fewer solutions in and around the grid are given higher priority. For example, as shown in Fig. 12, the objective space is divided into five segments in each dimension, with the ideal point located in the lower left corner of the square. All five solutions are non-dominated. For A and B, the grid coordinates are (0, 4) and (1, 4), and the distances of the grid from the ideal point (GR) are 4 and 5 (i.e., $0 + 4 = 4$, $1 + 4 = 5$). Because the GR of A is smaller than that of B, A is given a higher priority. Solutions B and C are in the same grid, and both have a GR of 5; however, B is given a higher priority because it is closer to the endpoint. To increase diversity, E is given a higher priority than A because more solutions exist in the grid near A.
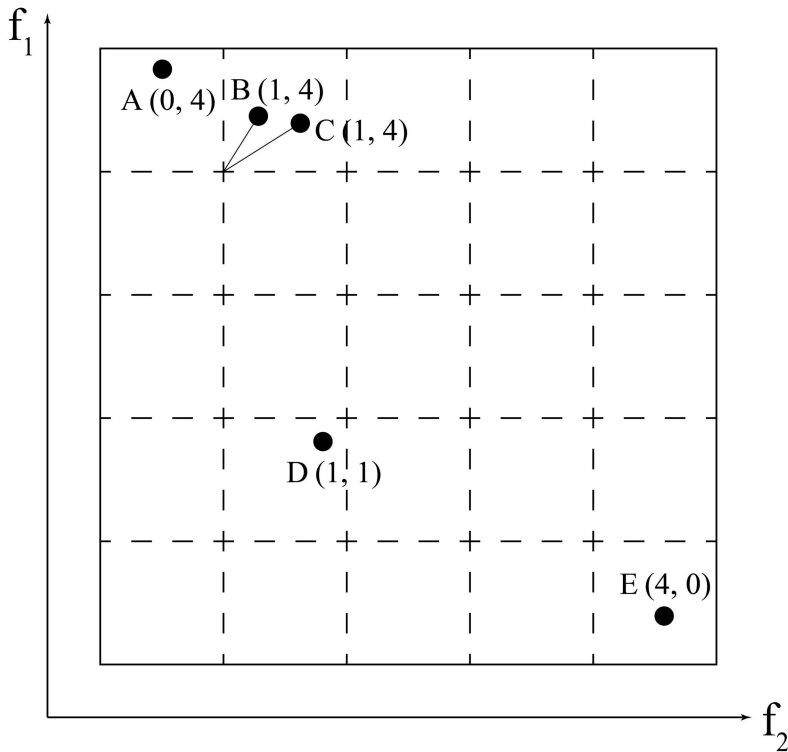

Fig. 12. Illustration of solutions in a two-dimensional objective space divided into a specified number of grids.

Instead of finding a suitable hyperplane in a complex objective space, using uniformly distributed grids to achieve a good balance between convergence and diversity is highly effective and robust. However, this leads to a distribution of converged solutions of the GrEA near the vertices of the different grids near the ideal point. Specifically, the distribution of solutions in hyperspace is a series of independent blocks rather than a uniform surface. As shown in Figs. 6 and 13, the Pareto front consisted of many inhomogeneous blocks. The GrEA exhibited good parallelism and can be easily used for

massive parallel computations. The computation time of the GrEA was almost negligible compared to that of the complex physical simulations. The parameter that had the greatest impact on the GrEA was the number of divisions in each dimension, which is recommended to be set to nine for an unknown problem or a slightly higher (or lower) value when a good approximation of the Pareto front for the problem is too difficult to achieve [30].

## 5. Optimization results for the 6 GeV ring

Section 4 demonstrates that the GrEA exhibits outstanding performance. This section uses the GrEA to perform a multi-objective optimization of the 6 GeV ring. The second approach generated an initial population with a size of 1000, and the maximum number of iterations was 250. As shown in Fig. 13, the Pareto front started to change slightly and converged at the 200th generation. After convergence, the solutions were uniformly distributed in individual blocks, which agrees with the principle of GrEA.
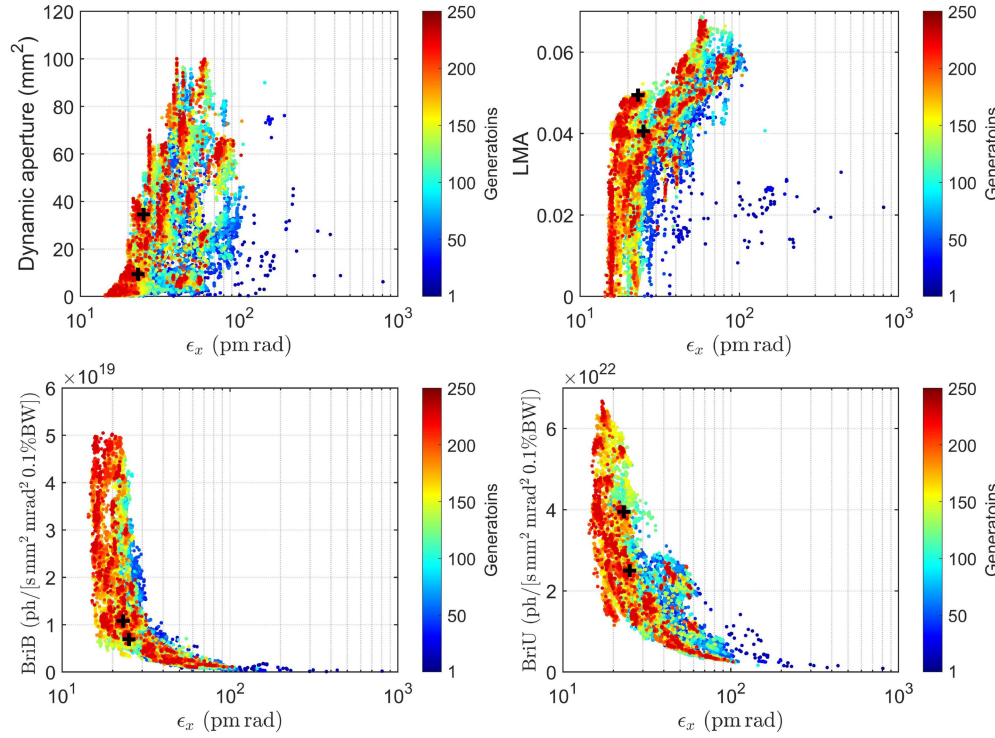

Fig. 13. Projection of Pareto front for different generations. Black crosses represent the two selected lattices.

As shown in Fig. 14, two representative lattices were chosen that had similar emittance, but the first lattice had a smaller value of the β_y function at the center of the straight section as well as at the

central dipole, which gave it a higher brilliance at these two locations but with a smaller dynamic aperture. As shown in Fig. 15, the horizontal dynamic aperture of the first lattice reached 2.1 mm while its vertical aperture reached 2.1 mm, and the horizontal aperture of the second lattice reached 4.5 mm while its vertical aperture reached 4.4 mm. They all had a certain dynamic aperture for particles with a ± 2 energy deviation. Figure 16 shows that both lattices had good LMAs, and the minimum LMAs in one cell were larger than 2%.
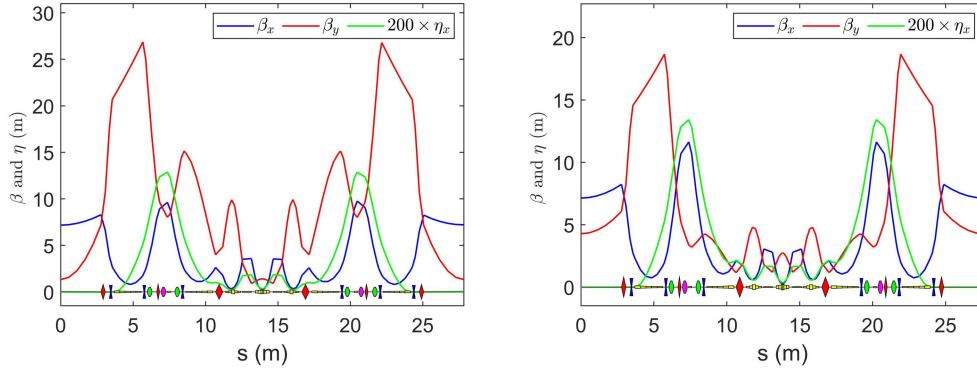
Fig. 14. Beam optics of the selected 6 GeV ring lattices, the first with a natural emittance of 23.08 pm·rad and circumference of 1336.25 m and the other with a natural emittance of 25.03 pm rad and circumference of 1327.21 m.
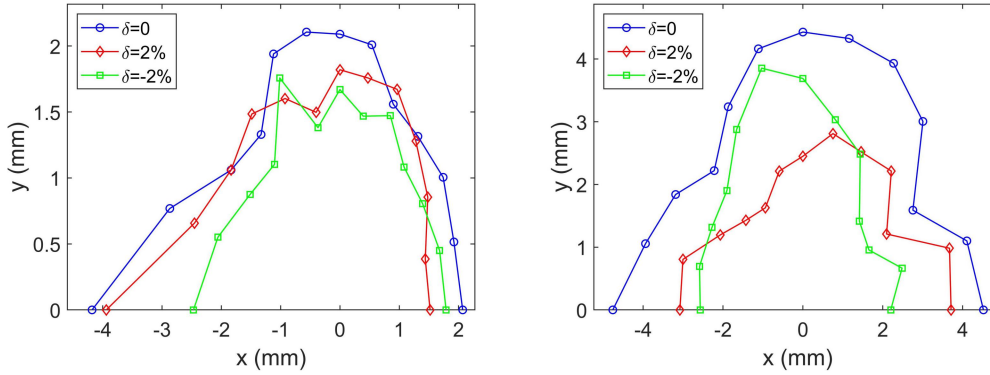
Fig. 15. Dynamic apertures of the two selected 6 GeV ring lattices with different energy deviations at the center of the straight section.
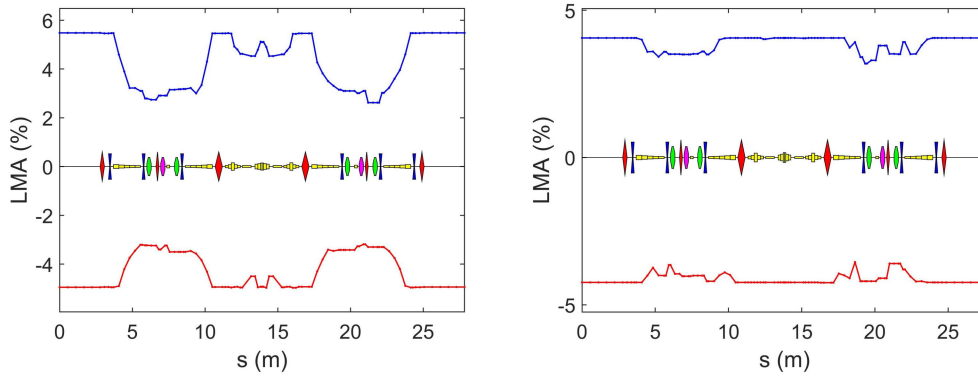
Fig. 16. Local momentum apertures within one cell of the two selected 6 GeV ring lattices.

6. Conclusion

Two ESRF-EBS-type lattices with different energies were designed for the experiments. The distribution of the initial population affected algorithm performance. For MaOPs with strict constraints and no preferences, increasing the number of randomly generated feasible solutions can enhance the diversity of the population and potentially improve the algorithm's performance. Three different MaOEAs and NSGA-II, a widely used MOEA, were used to perform multi-objective optimization of the 2 GeV ring. GrEA performed the best because of its ability to efficiently and robustly solve MaOPs. Owing to the complex shape of the objective space, the ASF used by NSGA-III to find a hyperplane failed in this optimization. After using MNDF as a substitute for ASF, NSGA-III performed better than NSGA-II but slightly worse than GrEA. MOEA/D could not handle the constraints well, showing an inability to maintain diversity and falling into local optima. Moreover, its performance was even worse than that of NSGA-II. Representative lattices with good attributes were selected from the GrEA results via feature extraction. GrEA was used to perform the many-objective optimization of the 6 GeV ring, and its application was demonstrated on two lattices with different beam optics at the center of the straight section and the central dipole.

This study uses MaOEAs for the first time to perform multi-objective optimization of DLSR lattices and illustrates that the GrEA is robust and performs well. Solutions with promising properties to satisfy all the objectives can be obtained for lattices with different energies. Therefore, this optimization strategy can be easily applied to other DLSRs prepared for construction or to other aspects of accelerators with more than three objectives.

Data Availability Statement

The data that support the findings of this study are openly available in Science Data Bank at

Author Contributions

All authors contributed to the study conception and design. He-Xing Yin performed the experiments. Jia-Bao Guan performed part of the experiments. Shun-Qiang Tian guided some physical aspects of the experiments. Ji-Ke Wang contributed to the conception of the study and key revisions of the manuscript. The first draft of the manuscript was written by He-Xing Yin and all authors commented on previous versions of the manuscript. All authors read and approved the final manuscript.

References

1. X.-Z. Liu, S.-Q. Tian, X. Wu, et al., Intra-beam scattering and beam lifetime in a candidate lattice of the soft X-ray diffraction-limited storage ring for the upgraded SSRF, Nucl. Sci. Tech., **32**, 83 (2021). https://doi.org/10.1007/s41365-021-00913-y

2. W. Gao, L. Wang, W. Li, Simultaneous optimization of beam emittance and dynamic aperture for electron storage ring using genetic algorithm, Phys. Rev. ST Accel. Beams, **14**, 094001 (2011). https://doi.org/10.1103/PhysRevSTAB.14.094001

3. R. Husain, A. Ghodke, Constrained multi-objective optimization of storage ring lattices, Nucl. Instrum. Methods Phys. Res., Sect. A, **883**, 151-158 (2018). https://doi.org/10.1016/j.nima.2017.11.077

4. D.S. Robin, W. Wan, F. Sannibale, et al., Global analysis of all linear stable settings of a storage ring lattice, Phys. Rev. ST Accel. Beams, **11**, 024002 (2008). https://doi.org/10.1103/PhysRevSTAB.11.024002

5. L. Yang, D. Robin, F. Sannibale, et al., Global optimization of an accelerator lattice using multiobjective genetic algorithms, Nucl. Instrum. Methods Phys. Res., Sect. A, **609**, 50-57 (2009). https://doi.org/10.1016/j.nima.2009.08.027

6. Y. Li, L. Yang, Multi-objective dynamic aperture optimization for storage rings, Int. J. Mod. Phys. A, **31**, 1644019 (2016). https://doi.org/10.1142/S0217751X1644019X

7. Y. Lu, S.C. Leemann, C. Sun, et al., Demonstration of machine learning-enhanced multi-objective optimization of ultrahigh-brightness lattices for 4th-generation synchrotron light sources, Nucl. Instrum. Methods Phys. Res., Sect. A, **1050**, 168192 (2023). https://doi.org/10.1016/j.nima.2023.168192

8. Z.-Y. Dai, Y.-C. Nie, Z. Hui, et al., Design of S-band photoinjector with high bunch charge and low

emittance based on multi-objective genetic algorithm, Nucl. Sci. Tech., **34**, 41 (2023). https://doi.org/10.1007/s41365-023-01183-6

9. Y. Zhao, Y. Jiao, S. Wang, Design study of APS-U-type hybrid-MBA lattice for mid-energy DLSR, Nucl. Sci. Tech., **32**, 71 (2021). https://doi.org/10.1007/s41365-021-00902-1

10. Z.-H. Bai, L. Wang, Q.-K. Jia, et al., Lattice study for the HLS-storage ring, Chin. Phys. C, **37**, 047004 (2013). https://doi.org/10.1088/1674-1137/37/4/047004

11. S.-C. Wang, D.-Y. He, C. Meng, et al., Development and simulation of a gridded thermionic cathode electron gun for a high-energy photon source, Nucl. Sci. Tech., **34**, 39 (2023). https://doi.org/10.1007/s41365-023-01195-2

12. Y. Jiao, G. Xu, X.-H. Cui, et al., The HEPS project, J. Synchrotron Radiat., **25**, 1611-1618 (2018). https://doi.org/10.1107/S1600577518012110

13. Y. Jiao, G. Xu, Optimizing the lattice design of a diffraction-limited storage ring with a rational combination of particle swarm and genetic algorithms, Chin. Phys. C, **41**, 027001 (2017). https://doi.org/10.1088/1674-1137/41/2/027001

14. K. Deb, A. Pratap, S. Agarwal, et al., A fast and elitist multiobjective genetic algorithm: NSGA-II, IEEE Trans. Evol. Comput., **6**, 182-197 (2002). https://doi.org/10.1109/4235.996017

15. E. Zitzler, M. Laumanns, L. Thiele, SPEA2: Improving the strength Pareto evolutionary algorithm, TIK-report, **103**, (2001). https://doi.org/10.1145/2851613.2851667

16. Z. He, G.G. Yen, J. Zhang, Fuzzy-based Pareto optimality for many-objective evolutionary algorithms, IEEE Trans. Evol. Comput., **18**, 269-285 (2013). https://doi.org/10.1109/TEVC.2013.2258025

17. M. Elarbi, S. Bechikh, A. Gupta, et al., A new decomposition-based NSGA-II for many-objective optimization, IEEE Trans. Syst. Man Cybern.: Syst., **48**, 1191-1210 (2017). https://doi.org/10.1109/TSMC.2017.2654301

18. B. Li, J. Li, K. Tang, et al., Many-objective evolutionary algorithms: A survey, ACM Computing Surveys (CSUR), **48**, 1-35 (2015). https://doi.org/10.1145/2792984

19. C.R. Raquel, P.C. Naval Jr, An effective use of crowding distance in multiobjective particle swarm optimization, in *Proceedings of the 7th Annual conference on Genetic and Evolutionary Computation,* 257-264 (2005). https://doi.org/10.1145/1068009.1068047

20. C. von Lücken, C. Brizuela, B. Barán, An overview on evolutionary algorithms for many – objective optimization problems, Wiley Interdiscip. Rev.: Data Min. Knowl. Discovery, **9**, e1267 (2019). https://doi.org/10.1002/widm.1267

21. S. Bechikh, M. Elarbi, L.B. Said, Many-objective optimization using evolutionary algorithms: A

survey, in: *Recent advances in evolutionary multi-objective optimization*, (Springer, 2017), pp. 105-137. https://doi.org/10.1007/978-3-319-42978-6_4

22. Y. Zhou, J. Wang, J. Chen, et al., Ensemble of many-objective evolutionary algorithms for many-objective problems, Soft Computing, **21**, 2407-2419 (2017). https://doi.org/10.1007/s00500-015-1955-3

23. K. Deb, H. Jain, An evolutionary many-objective optimization algorithm using reference-point-based nondominated sorting approach, part I: solving problems with box constraints, IEEE Trans. Evol. Comput., **18**, 577-601 (2013). https://doi.org/10.1109/TEVC.2013.2281535

24. J. Yan, H. Deng, Generation of large-bandwidth x-ray free electron laser with evolutionary many-objective optimization algorithm, Phys. Rev. Accel. Beams, **22**, 020703 (2019). https://doi.org/10.1103/PhysRevAccelBeams.22.020703

25. H. Ishibuchi, R. Imada, Y. Setoguchi, et al., Performance comparison of NSGA-II and NSGA-III on various many-objective test problems, in *2016 IEEE Congress on Evolutionary Computation (CEC),* 3045-3052 (2016). https://doi.org/10.1109/CEC.2016.7744174

26. X. Huang, J. Safranek, Nonlinear dynamics optimization with particle swarm and genetic algorithms for SPEAR3 emittance upgrade, Nuclear Instruments and Methods in Physics Research Section A Accelerators Spectrometers Detectors and Associated Equipment, **757**, 48–53 (2014). https://doi.org/10.1016/j.nima.2014.04.078

27. P. Raimondi, ESRF-EBS: The extremely brilliant source project, Synchrotron Radiat. News, **29**, 8-15 (2016). https://doi.org/10.1080/08940886.2016.1244462

28. A. Streun, The anti-bend cell for ultralow emittance storage ring lattices, Nucl. Instrum. Methods Phys. Res., Sect. A, **737**, 148-154 (2014). https://doi.org/10.1016/j.nima.2013.11.064

29. A. Streun, A. Wrulich, Compact low emittance light sources based on longitudinal gradient bending magnets, Nucl. Instrum. Methods Phys. Res., Sect. A, **770**, 98-112 (2015). https://doi.org/10.1016/j.nima.2014.10.002

30. S. Yang, M. Li, X. Liu, et al., A grid-based evolutionary algorithm for many-objective optimization, IEEE Trans. Evol. Comput., **17**, 721-736 (2013). https://doi.org/10.1109/TEVC.2012.2227145

31. Q. Zhang, H. Li, MOEA/D: A multiobjective evolutionary algorithm based on decomposition, IEEE Trans. Evol. Comput., **11**, 712-731 (2007). https://doi.org/10.1109/TEVC.2007.892759

32. I. Das, J.E. Dennis, Normal-boundary intersection: A new method for generating the Pareto surface in nonlinear multicriteria optimization problems, SIAM J. Optim., **8**, 631-657 (1998). https://doi.org/10.1137/S1052623496307510

33. K. Miettinen, J. Hakanen, D. Podkopaev, Interactive nonlinear multiobjective optimization methods, in: *Multiple criteria decision analysis*, (Springer, 2016), pp. 927-976. https://doi.org/10.1007/978-

1-4939-3094-4_22

34. M. Ming, R. Wang, Y. Zha, et al., Pareto adaptive penalty-based boundary intersection method for multi-objective optimization, Inf. Sci., **414**, 158-174 (2017). https://doi.org/10.1016/j.ins.2017.05.012

35. H. Ishibuchi, N. Tsukamoto, Y. Nojima, Evolutionary many-objective optimization: A short review, in *2008 IEEE congress on evolutionary computation (IEEE world congress on computational intelligence), Hong Kong, China,* 2419-2426 (2008). https://doi.org/10.1109/CEC.2008.4631121

36. H. Ishibuchi, H. Masuda, Y. Tanigaki, et al., Modified distance calculation in generational distance and inverted generational distance, in *International conference on evolutionary multi-criterion optimization,* 110-125 (2015). https://doi.org/10.1007/978-3-319-15892-1_8

37. S. Jiang, J. Zhang, Y.-S. Ong, et al., A simple and fast hypervolume indicator-based multiobjective evolutionary algorithm, IEEE Trans. Cybern., **45**, 2202-2213 (2014). https://doi.org/10.1109/TCYB.2014.2367526

38. R. Bartolini, G. Cinque, K. Sawhney, et al., Concepts for a low emittance-high capacity storage ring for the Diamond light source, 2016.

39. C. Steier, A. Allézy, A. Anders, et al., Status of the conceptual design of ALS-U, in *9th International Particle Accelerator Conference,* 4134-4137 (2018). http://dx.doi.org/10.18429/JACOW-IPAC2017-WEPAB104

40. M. Dehler, A. Citterio, T. Garvey, et al., Conceptual Design for SLS-2, in *60th ICFA Advanced Beam Dynamics Workshop on Future Light Sources (FLS'18), Shanghai, China,* (2018).

41. J. Citadini, L.N. Vilela, R. Basilio, et al., Sirius-details of the new 3.2 T permanent magnet Superbend, IEEE Trans. Appl. Supercond., **28**, 1-4 (2017). https://doi.org/10.1109/TASC.2017.2786270

42. H. Li, J. Wang, L. Tang, et al., Project of Wuhan Photon Source, in *Proceedings of the 12th International Particle Accelerator Conference (IPAC 2021). Online Conference,* 346-349 (2021). https://doi.org/10.18429/JACoW-IPAC2021-MOPAB092

43. A. Terebilo, Accelerator toolbox for MATLAB, Citeseer, 2001.

44. K.J. Kim, Optical and power characteristics of synchrotron radiation sources, Opt. Eng., **34**, 342-352 (1995).

45. J. Wan, P. Chu, Y. Jiao, Neural network-based multiobjective optimization algorithm for nonlinear beam dynamics, Phys. Rev. Accel. Beams, **23**, 081601 (2020). https://doi.org/10.1103/PhysRevAccelBeams.23.081601

46. J. Wan, P. Chu, Y. Jiao, et al., Improvement of machine learning enhanced genetic algorithm for nonlinear beam dynamics optimization, Nucl. Instrum. Methods Phys. Res., Sect. A, **946**, 162683

(2019). https://doi.org/10.1016/j.nima.2019.162683

47.   A.B. Ruiz, R. Saborido, M. Luque, A preference-based evolutionary algorithm for multiobjective optimization: the weighting achievement scalarizing function genetic algorithm, J. Global Optim., **62**, 101-129 (2015). https://doi.org/10.1007/s10898-014-0214-y

48.   J. Blank, K. Deb, P.C. Roy, Investigating the normalization procedure of NSGA-III, in *International Conference on Evolutionary Multi-Criterion Optimization,* 229-240 (2019). https://doi.org/10.1007/978-3-030-12598-1_19